

Influence of foam on the stability characteristics of immiscible flow in porous media

van der Meer, Jakolien; Farajzadeh, Rouhi; Rossen, Bill; Jansen, Jan Dirk

DOI

[10.1063/1.5000891](https://doi.org/10.1063/1.5000891)

Publication date

2018

Document Version

Final published version

Published in

Physics of Fluids

Citation (APA)

van der Meer, J., Farajzadeh, R., Rossen, B., & Jansen, J. D. (2018). Influence of foam on the stability characteristics of immiscible flow in porous media. *Physics of Fluids*, 30(1), Article 014106. <https://doi.org/10.1063/1.5000891>

Important note

To cite this publication, please use the final published version (if applicable). Please check the document version above.

Copyright

Other than for strictly personal use, it is not permitted to download, forward or distribute the text or part of it, without the consent of the author(s) and/or copyright holder(s), unless the work is under an open content license such as Creative Commons.

Takedown policy

Please contact us and provide details if you believe this document breaches copyrights. We will remove access to the work immediately and investigate your claim.

Green Open Access added to TU Delft Institutional Repository

'You share, we take care!' – Taverne project

<https://www.openaccess.nl/en/you-share-we-take-care>

Otherwise as indicated in the copyright section: the publisher is the copyright holder of this work and the author uses the Dutch legislation to make this work public.

Influence of foam on the stability characteristics of immiscible flow in porous media

J. M. van der Meer,^{a)} R. Farajzadeh,^{b)} W. R. Rossen, and J. D. Jansen

Department of Geosciences and Engineering, Delft University of Technology, Delft 2628 CN, The Netherlands

(Received 19 August 2017; accepted 19 December 2017; published online 26 January 2018)

Accurate field-scale simulations of foam enhanced oil recovery are challenging, due to the sharp transition between gas and foam. Hence, unpredictable numerical and physical behavior is often observed, casting doubt on the validity of the simulation results. In this paper, a thorough stability analysis of the foam model is presented to validate the simulation results. We study the effect of a strongly non-monotonous total mobility function arising from foam models on the stability characteristics of the flow. To this end, we apply the linear stability analysis to nearly discontinuous relative permeability functions and compare the results with those of highly accurate numerical simulations. In addition, we present a qualitative analysis of the effect of different reservoir and fluid properties on the foam fingering behavior. In particular, we consider the effect of heterogeneity of the reservoir, injection rates, and foam quality. Relative permeability functions play an important role in the onset of fingering behavior of the injected fluid. Hence, we can deduce that stability properties are highly dependent on the non-linearity of the foam transition. The foam-water interface is governed by a very small total mobility ratio, implying a stable front. The transition between gas and foam, however, exhibits a huge total mobility ratio, leading to instabilities in the form of viscous fingering. This implies that there is an unstable pattern behind the front. We deduce that instabilities are able to grow behind the front but are later absorbed by the expanding wave. Moreover, the stability analysis, validated by numerical simulations, provides valuable insights about the important scales and wavelengths of the foam model. In this way, we remove the ambiguity regarding the effect of grid resolution on the convergence of the solutions. This insight forms an essential step toward the design of a suitable computational solver that captures all the appropriate scales, while retaining computational efficiency. *Published by AIP Publishing.* <https://doi.org/10.1063/1.5000891>

I. INTRODUCTION

Foam enhanced oil recovery (EOR) is applied to increase oil production by reducing disadvantageous effects like channeling, viscous fingering, and gravity override. When gas is injected into a porous medium containing a surfactant solution, a foam front forms. The foam captures the gas in bubbles and reduces its mobility. The effectiveness of the process depends on the stability of the created foam controlled by the magnitude of the capillary pressure. It has been observed that foam experiences a significant coalescence when the capillary pressure approaches the so-called limiting capillary pressure, P_c^* .^{9,12} In other words, when the water saturation drops below a critical value, called the limiting water saturation S_w^* , foam becomes too dry and collapses. The mobility of the gas, which is the ratio of the relative gas permeability and the gas viscosity, therefore contains a sharp transition around the limiting water saturation.

To reduce the operational risks associated with injectivity decline because of generation of very strong foams, material

compatibility, and well integrity, it has been suggested to inject gas and surfactant solution into an alternating mode, i.e., a slug (fraction of the pore volume) of surfactant followed by a slug of gas. Upon mixing of the gas and the surfactant solution in the pores, foam lamellae will form *in situ*. Behind the foam front, gas reduces the water saturation to saturations close to the limiting water saturation and therefore with gradual or abrupt collapse of foam, the gas mobility increases from the foam front toward the injection well. The instabilities that might occur within this bank (between the front and the injection point) have been the subject of a recent study,¹⁰ which suggested that the fingering has a physical origin and is not due to numerical artifacts discussed in the paper. This phenomenon, the extent of which depends mainly on the properties of the foam behind the front, may not be visible in simulations with poor grid resolutions.

Because of this aspect of foam, accurate field-scale simulations are challenging. Hence, unpredictable numerical and physical behavior is often observed, casting doubt on the validity of the simulation results.^{2,3,5,10,15} In this paper, a thorough stability analysis of an implicit texture (local equilibrium) foam model is presented to validate the simulation results and lay a foundation for a tailor-made solver, which can both handle large-scale reservoir simulations and accurately resolve front instabilities. We study the effect of a strongly non-monotonous total mobility function, arising from foam

Note: This manuscript is an extended version of a paper presented at the SPE Reservoir Simulation Conference held in Montgomery, Texas, USA, 20-22 February 2017.

^{a)}Electronic mail: j.m.vandermeer@tudelft.nl.

^{b)}Also at Shell Global Solutions International, Rijswijk, The Netherlands.

models, on the stability characteristics of the flow. To this end, we generalize the linear stability analysis of Yortsos and Hickernell,²⁹ Riaz *et al.*,²⁰ Riaz and Tchelepi,^{16,17,19} and Meulenbroek *et al.*¹⁴ to nearly discontinuous relative permeability functions and compare the results with those of highly accurate numerical simulations.

In this earlier work on the stability of immiscible two-phase flow in porous media, a linear stability analysis was performed for the quasi-linearized model. This was done in a transformed coordinate frame that moves along with the front. By using a perturbation theory that exploits a normal mode decomposition strategy, it was shown that the onset of the instabilities of the displacing fluid is governed by the total mobility ratio across the shock (as opposed to the mobility ratio over the entire transition region). The shape of the relative permeability curves plays an important role at this stage.¹⁷

We therefore propose to apply the perturbation theory to the foam model, in order to investigate the effect of the abrupt changes in the gas relative permeability on the stability of the foam front. We are especially interested in the effect of this particular relative permeability function on the stability characteristics of the model. The function form differs from the ones described by Riaz and Tchelepi¹⁷ because it allows for discontinuities and the corresponding total mobility function is non-monotonic and can have an unfavorable shock-mobility ratio.

The foam-water interface has usually a very small total mobility ratio, leading to a stable front. The subsequent transition front, where foam turns into gas, exhibits a large total mobility ratio. This implies that there is an unstable pattern behind the front, which can be detected by highly accurate numerical simulations. An indication of this behavior was shown in the study of Farajzadeh *et al.*¹⁰ for a two-phase incompressible immiscible foam model.

The question is to which extent the strong non-linearities in the foam model can be described by a linear stability analysis. To answer this, we compare the linear stability results with accurate numerical simulations, where we approximate several properties, such as the interfacial length, wave number, and maximum growth number. To solve the system of saturation and pressure equations, we apply a semi-implicit finite volume method. To minimize numerical diffusion around the front, we use a second-order monotonic upstream-centered scheme for conservation laws (MUSCL) for the hyperbolic flux functions and a central scheme to compute the pressure values. Both equations contain a strongly non-linear mobility function, and therefore the system is considered stiff. Hence, the time step of the numerical scheme is very restricted, and the numerical scheme exhibits stability issues. To improve the stability of the numerical scheme, a Taylor-Galerkin method is applied to the entire system. The non-linearity is accounted for by introducing auxiliary variables.¹ Using this scheme, we are able to resolve the very fast wave speeds that emerge from the non-linearity of the model.

The structure of the paper is as follows: first, we introduce the two-phase foam model and discuss its characteristics in Sec. II. For this model, a linear stability analysis is performed in Sec. III. The results from this analysis, listed

in Sec. IV, are then compared to numerical simulations discussed in Secs. VI and VII. Finally, we discuss the outcomes of both analyses in Sec. VIII.

II. FOAM MODEL

We use the non-dimensional model described by Ref. 19 for the injection of an incompressible gas into a porous rock initially filled with water, which is given by

$$\begin{aligned} \partial_t S &= -\nabla \cdot \left(\frac{Mk_{rg}}{\lambda} \mathbf{u} + G \frac{k_{rg}k_{rw}}{\lambda} \nabla z + \frac{k_{rg}k_{rw}}{N_{ca}\lambda} \frac{dP_c}{dS_w} \nabla S \right) \\ &= -\nabla \cdot (k_{rw} \nabla \bar{P}), \end{aligned} \quad (1)$$

$$\nabla \mathbf{u} = 0, \quad (2)$$

$$\mathbf{u} = -\lambda \nabla \bar{P} + Gk_{rg} \nabla z + \frac{1}{N_{ca}} k_{rg} \frac{dP_c}{dS_w} \nabla S, \quad (3)$$

where $S = (S_g - S_{gr})/(1 - S_{wc} - S_{gr})$ is the normalized gas saturation,

$$\nabla \bar{P} = \nabla P_w + (\rho_w g k / \mu_w U) \nabla z \quad (4)$$

is the derivative of the scaled pressure \bar{P} , $P_c = P_w - P_g$ is the capillary pressure, u is the total Darcy velocity, and $\lambda = Mk_{rg} + k_{rw}$ is the dimensionless mobility function. Here, $k_{r\alpha}$ denote the relative permeability functions of phase $\alpha \in w, g$, which are defined later. The variables M , G , and N_{ca} denote the dimensionless end point mobility ratio, gravity number, and capillary number, respectively, which are given by

$$M = \frac{\mu_w k_{rge}}{\mu_g k_{rwe}}, \quad (5)$$

$$G = \frac{k\Delta\rho g}{\mu_g U}, \quad (6)$$

$$N_{ca} = \frac{\mu_g U W}{\gamma_{gw} \sqrt{\phi k}}, \quad (7)$$

where W is a characteristic length scale of the model where viscous and capillary terms are of comparable magnitude²⁹ and U is a characteristic velocity, which is set equal to the gas injection rate divided by a unit surface area. The other parameters are explained in Appendix A. We consider the one-dimensional version of this equations with $\mathbf{u} = 1$, given by

$$\partial_t S + \partial_x \left(f(S) + \frac{k_{rg}k_{rw}}{N_{ca}\lambda} \frac{dP_c}{dS_w} \frac{dS}{dx} \right) = 0. \quad (8)$$

If capillary pressure is neglected ($Ca \rightarrow \infty$), this equation is the Buckley-Leverett equation with a non-convex flux

$$f = \frac{Mk_{rg}}{\lambda} \left(1 + G \frac{k_{rw}}{M} \right), \quad (9)$$

for which we can derive the characteristic solution. The characteristics of this solution depend on the form of the normalized relative permeability functions k_{rw} and k_{rg} , which are given by

$$k_{rg} = \frac{S_g^{n_g}}{f_{mr}}, \quad f_{mr} = 1 + R \cdot F_w, \quad (10)$$

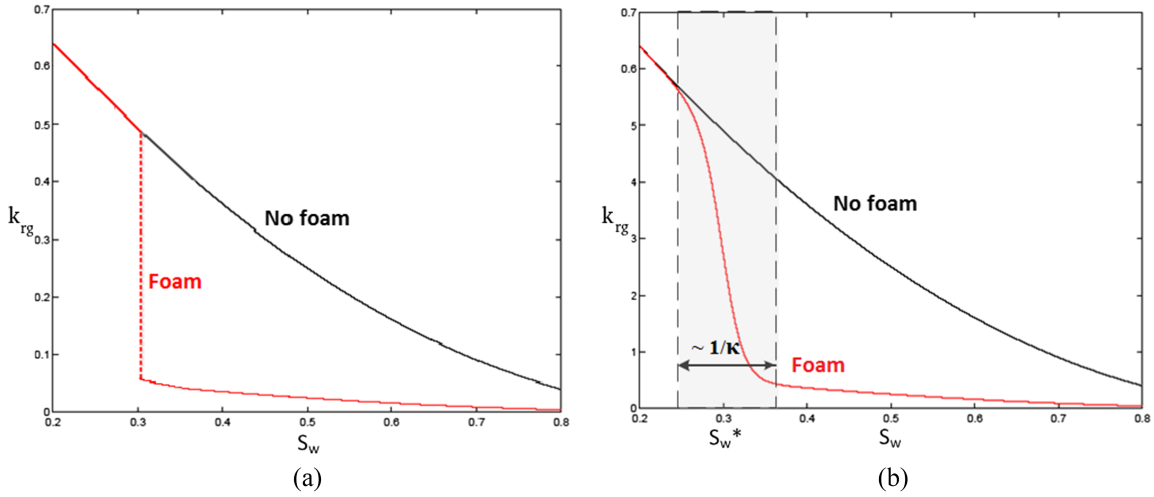


FIG. 1. Relative permeability function of the local-equilibrium foam model with foam present ($f_{mr} > 1$) and without foam present ($f_{mr} = 1$). The sudden drop in the relative permeability of gas, due to foam, is shown for different transition rates κ , for $S_w^* = 0.3$, $R = 10$, $M = 1$, and $G = 0$.²⁶ (a) $\kappa = \infty$, (b) $\kappa = 40$.

$$k_{rw} = (1 - S)^{n_w}, \quad (11)$$

where f_{mr} is the mobility reduction factor due to foam generation and R is a constant that accounts for the maximum

flow resistance of the foam. The function F_w describes the dependency of the foam strength to water saturation and is given by²³

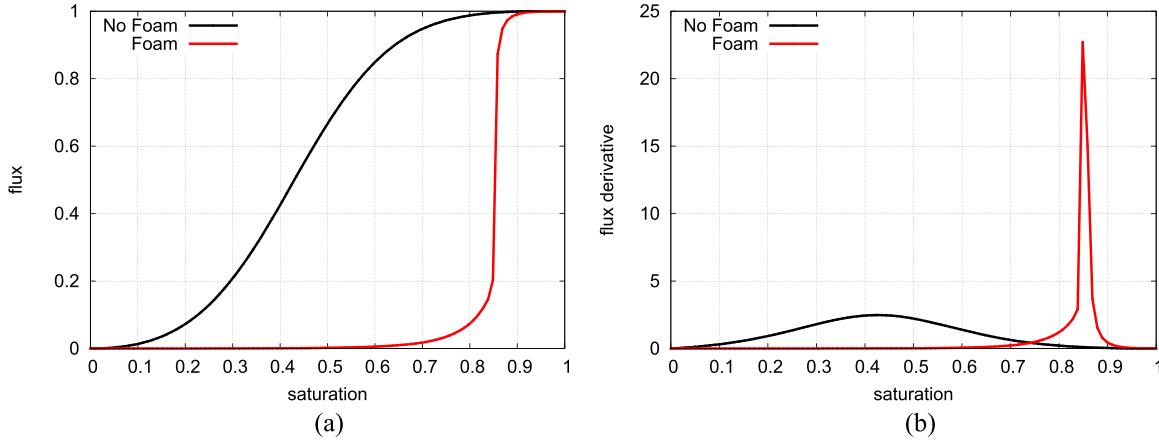


FIG. 2. Flux function and flux derivative of the local-equilibrium foam model with and without foam present, for $S_w^* = 0.15$, $\kappa = 1000$, $R = 1000$, $M = 1$, and $G = 0$.²⁶ (a) Flux, (b) flux derivative.

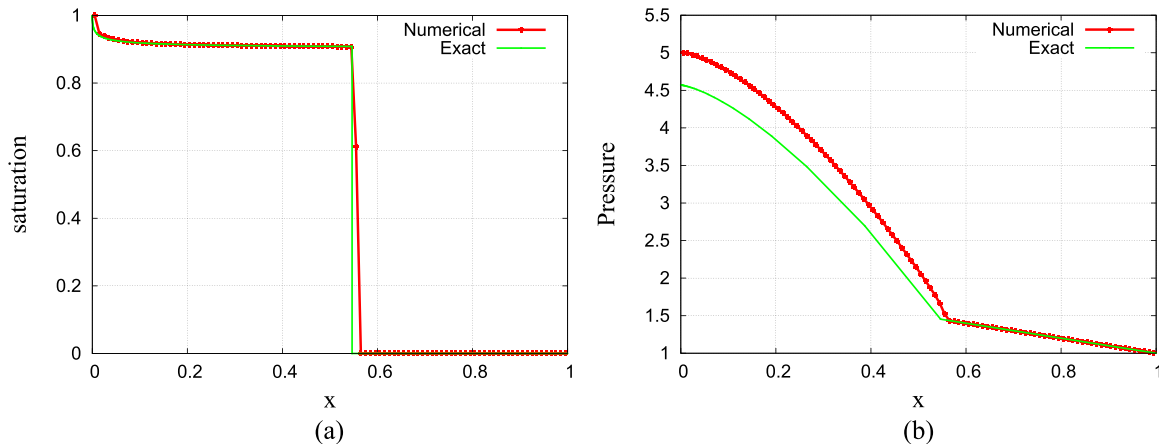


FIG. 3. Saturation and pressure solution of the Buckley-Leverett equation at $t = 0.05$, for $S_w^* = 0.1$, $\kappa = 1000$, $R = 10\,000$, $M = 1$, and $G = 0$. (a) Saturation, (b) pressure.

$$F_w = 0.5 + \frac{\arctan(\kappa(S_w - S_w^*))}{\pi}, \quad (12)$$

where S_w^* represents the limiting water saturation and κ is a positive parameter that controls the width of the gas-foam transition. For $\kappa = \infty$, the gas-foam transition is instant [Fig. 1(a)], and no foam exists below S_w^* . For smaller values of κ , the mobility reduction of foam (i.e., of the foam strength) increases as the water saturation increases in the transition zone [Fig. 1(b)]. In other words, foam collapse occurs over a range of water saturations whose width is determined by κ . The corresponding flux functions and derivatives are shown in Fig. 2.

The characteristic solution of the Buckley-Leverett equation for gas injection into a water saturated medium with the given relative permeability functions consists of a rarefaction and a right-moving shock wave²² as shown in Fig. 3. The shock-speed v_s can be determined from

$$v_s = \left. \frac{df(S)}{dS} \right|_{S_s} = \frac{f(S_s) - f(S_i)}{S_s - S_i}, \quad (13)$$

where S_s is the shock saturation and $S_i = 0$ is the initial gas saturation in the porous medium. For saturation values larger than S_s , the solution consists of a rarefaction wave, for which $x/t = f'(S(x, t))$.¹³

III. LINEAR STABILITY ANALYSIS

To analyze the influence of foam on the stability characteristics of the fluid displacement, we perform a linear stability analysis on Eqs. (1) and (2), where we start off with the full system including capillarity. To do so, we linearize the equations around a base state that is given by the characteristic solution of the one-dimensional version of the saturation equation, Eq. (8). For this equation, a self-similar solution exists as a function of $\xi = x - v_s t$, in the neighborhood of the Buckley-Leverett shock where $\xi = 0$, which does not change in time.²⁹ This solution can be used as the base state (S_0, P_0) for the stability analysis,¹⁹ which is given by

$$\frac{dS_0}{d\xi} = \frac{\lambda Ca}{k_{rw} k_{rg} P'_c} (v_s S_0 - f(S_0)), \quad (14)$$

$$\frac{dP_0}{d\xi} = \frac{1}{\lambda} \left(Gk_{rg} + \frac{k_{rg}}{Ca} P'_c S'_0 - 1 \right). \quad (15)$$

In the absence of capillarity ($Ca \rightarrow \infty$), the base state satisfies

$$\frac{S_0}{d\xi} = \delta(\xi), \quad (16)$$

$$\frac{dP_0}{d\xi} = \frac{Gk_{rg} - 1}{\lambda}. \quad (17)$$

We can expand the full solution in terms of the base state and a perturbation function.¹⁹ The last is written as a set of stream-wise eigenfunctions \hat{s} and \hat{p} times a normal mode series, such that

$$(S, P)(\xi, y, t) = (S_0, P_0)(\xi) + (\hat{s}, \hat{p})(\xi) e^{iny + \sigma t}, \quad (18)$$

where n denotes the wave number of the perturbation and σ denotes the wave growth rate. Substituting this eigenmode

expansion into Eqs. (1) and (2), and solving the resulting eigenvalue problem,^{16,19} leads to an expression for the disturbance velocity,

$$\frac{\sigma}{n} = \frac{f_{g1} - f_{g0}}{S_1 - S_0} \frac{\lambda_1(1 - Gk_{rg0}) - \lambda_0(1 - Gk_{rg1})}{\lambda_1 - \lambda_0}, \quad (19)$$

where the subscripts 0 and 1 denote the front and back edges of the shock, respectively. The derivation of these equations can be found in Appendix B. If there is no gravity influence ($G = 0$), i.e., if we consider a horizontally located reservoir, this becomes

$$\frac{\sigma}{n} = \frac{f_{g1} - f_{g0}}{S_1 - S_0} = v_s \Lambda, \quad (20)$$

$$\Lambda = \frac{M_s - 1}{M_s + 1}, \quad (21)$$

where $M_s = \lambda_1/\lambda_0$, the mobility ratio across the shock, and Λ is the disturbance number. Hence we see that this number is positive if $M_s > 1$, which means that the flow is unstable at the shock. Vice versa, a mobility ratio smaller than one leads to a stable displacement. If gravity is included, it has been shown by Ref. 19 that

$$G(k_{rg1} - M_s k_{rg0}) < 1 - M_s \quad (22)$$

to obtain stable displacement. If capillarity is included, apart from the shock mobility ratio, the fractional flow profiles have an influence on the stability of the flow. In the limit of small wave numbers, the disturbance velocity can therefore be extended to a higher-order formulation²⁹ given by

$$\sigma = \Gamma_1 n + \Gamma_2 n^2 + \Gamma_3 \ln(n(s_1 - s_0)) n^2, \quad (23)$$

where Γ_1 is given by Eq. (19) and Γ_2 and Γ_3 are determined by the derivative of the total mobility and the fractional flow profiles.

IV. STABILITY CHARACTERISTICS

The above analysis for the model without capillarity and gravity allows us to investigate the influence of foam on the viscous instability at the front. Based on the results of Farajzadeh *et al.*,¹⁰ different scenarios are addressed: a weak foam (low mobility reduction factor, case 1), three cases of a strong foam (high mobility reduction factor, case 2–4) with different transition lengths from foam to gas (see Fig. 4), and a fifth case with the effect of gravity included.

Since we only looked at the linearized model without capillarity, there is no damping at large wave numbers,¹⁹ and hence the wave growth is a linear increasing function of the wave number. Moreover, the base state of the model without capillarity contains a shock wave at $S_0 = S_s = \max_S \frac{f_g(S) - f_g(S_R)}{S - S_R}$, which marks the interface between gas and water. The shock wave is followed by a rarefaction wave, where water and gas co-exist. As shown in Fig. 5(a), the shock saturation of water (gas) is almost everywhere smaller (larger) than the limiting water (gas) saturation, i.e., the saturation that marks the transition from gas to foam. Therefore, only due to a numerically and/or physically dispersed shock (denoted by red dashed lines), or a very wide transition range of foam (denoted by blue dashed lines), foam can exist in this model. The second plot [Fig. 5(b)]

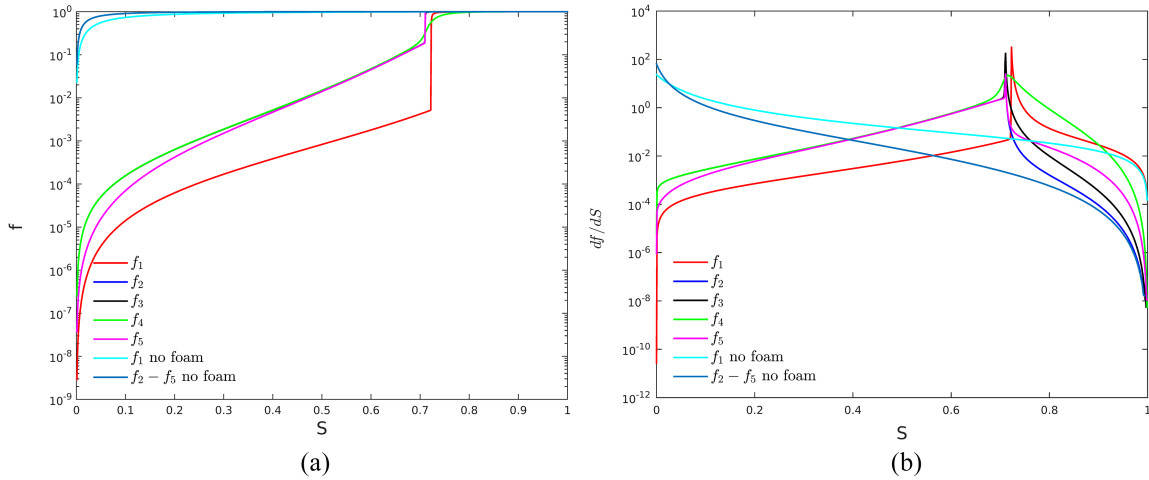


FIG. 4. (a) Flux functions and (b) flux derivative/wave speed of the five test cases of Farajzadeh *et al.*¹⁰ and two reference cases without foam.

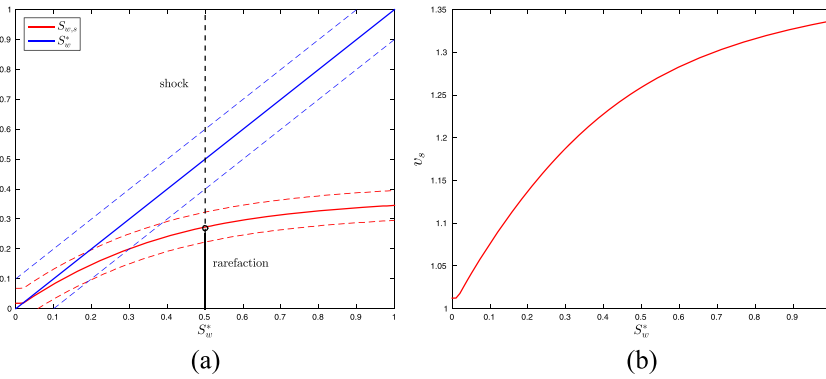


FIG. 5. (a) Shock saturation, S_s , versus the limiting water saturation, S_w^* , for $\kappa = 1000$, $R = 1000$, and $G = 0$. (b) Shock speed, v_s , versus the limiting water saturation, for $\kappa = 1000$, $R = 1000$, and $G = 0$. The red dashed lines indicate the diffusion around the shock because of capillarity and/or numerical diffusion. The blue dashed lines indicate the transition width of the foam, which is governed by the inverse of κ .

shows that the shock speed increases with the limiting water saturation because strong foam slows down the front significantly. It follows from Eq. (20) that the viscous instability increases linearly with the shock speed. Thus, strong foam has less instabilities than weak foam, according to this analysis. This corresponds to the results obtained by Farajzadeh *et al.*¹⁰

We can also examine the influence of the mobility ratio on the growth rate of the various test cases described in the study of Farajzadeh *et al.*,¹⁰ as depicted in Fig. 6(a). As the mobility ratio increases, the growth rate also increases. For a small mobility ratio, the growth rate increases very fast for the fifth test case f_5 , after which it scales with approximately $M^{1/2}$, which is similar to what Riaz and Tchelepi¹⁶ observed for their

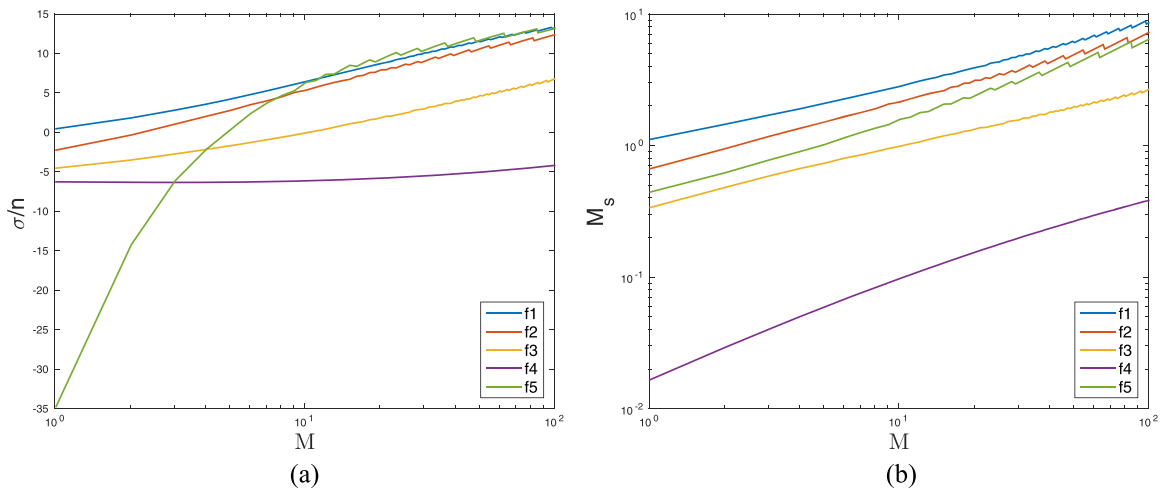


FIG. 6. (a) Growth rate versus the mobility ratio M and (b) total mobility ratio across the shock versus M , for the five test cases of Farajzadeh *et al.*¹⁰

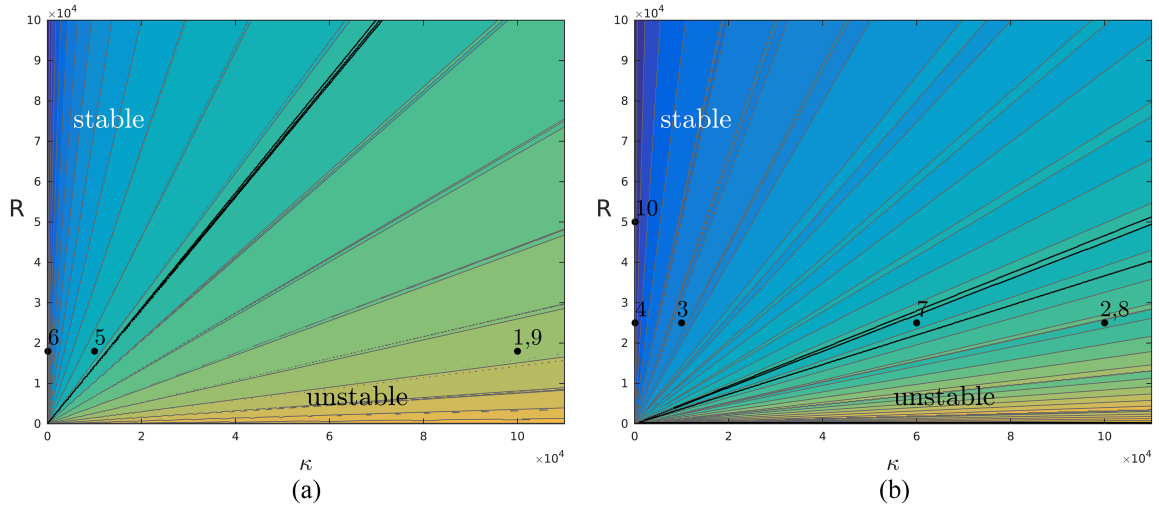


FIG. 7. Stability regions in the κ - R plane for the rest of the parameter set of (a) test case one and (b) test case two of Farajzadeh *et al.*¹⁰ The stable and unstable regions are separated by the thick black lines, and the different test cases are denoted by thick black dots.

test cases without foam. The first three cases including foam (denoted by f_1, f_2, f_3) show an overall increase of $M^{1/2}$, and the fourth test case f_4 has a more or less constant growth number which is always smaller than zero. This implies that the fourth test case is always stable, whereas the first test case is always unstable ($\sigma/n > 0$). The other three test cases are unstable at the shock front for larger mobility ratios only, according to this analysis. Also, if we have a look at the mobility ratio across the shock depicted in Fig. 6(b), we see the same pattern. For the fourth test case, the shock ratio $M_s < 1$ for all M , which is according to our expectations and implies a stable displacement for all values of M . For the first test case, $M_s > 1$ for all M , implying an unfavorable displacement, with instabilities. The other three test cases have unfavorable mobility ratios for values of $M > 10$. Moreover, for large viscosity ratios, we observe an oscillatory pattern due to the total mobility values,

which are very sensitive to small changes in the parameters [see Fig. 10(a)].

Since the foam models are characterized by the parameters R , κ , and S_w^* , we studied the influence of these parameters on the dimensionless growth number Λ . Figure 7 shows the contour lines of the growth number in the κ - R plane, for the remaining parameter sets of the test cases one and two of Farajzadeh *et al.*¹⁰ The stable region for the parameter set of the first parameter set defined in Table I is much larger than for the parameter set of the test case 2–4. This is probably an effect of the mobility ratio, which is larger for the second parameter set ($M_2 = 235$ vs $M_1 = 61$). We also observe that the stability contour lines, which are set by the dimensionless growth number, are all straight with a positive angle. This means that an increasing mobility reduction factor (R) has a stabilizing effect, while an increasing non-linearity (κ) has a destabilizing effect.

TABLE I. Simulation parameters for the four test cases of Farajzadeh *et al.*¹⁰

Parameter (unit)	Case 1	Case 2	Case 3	Case 4
Foam strength R	1.8×10^4	2.5×10^4	2.5×10^4	2.5×10^4
Critical saturation S_w^*	0.268	0.29	0.29	0.29
Foam transition width κ	10^5	10^5	10^4	10^2
End point gas permeability k_{rge}	0.94	0.94	0.94	0.94
End point water permeability k_{rwe}	0.2	0.2	0.2	0.2
Gas viscosity μ_g (Pa s)	5×10^{-5}	2×10^{-5}	2×10^{-5}	2×10^{-5}
Water viscosity μ_w (Pa s)	0.65×10^{-3}	10^{-3}	10^{-3}	10^{-3}
Power coefficient gas n_g	1.8	1.3	1.3	1.3
Power coefficient water n_w	2	4.2	4.2	4.2
Gas density ρ_g (kg/m ³)	10^{-5}	10^{-5}	10^{-5}	10^{-5}
Water density ρ_w (kg/m ³)	10^{-5}	10^{-5}	10^{-5}	10^{-5}
Residual gas saturation $S_{g,r}$	0.0	0.0	0.0	0.0
Residual water saturation $S_{w,c}$	0.0	0.0	0.0	0.0
Injected gas saturation $S_{g,inj}$	1.0	1.0	1.0	1.0
Injection rate gas I (m ³ /s)	3.5×10^{-5}	3.5×10^{-5}	3.5×10^{-5}	3.5×10^{-5}
Absolute permeability K (m ²)	5×10^{-10}	5×10^{-10}	5×10^{-10}	5×10^{-10}
Porosity ϕ	0.2	0.2	0.2	0.2

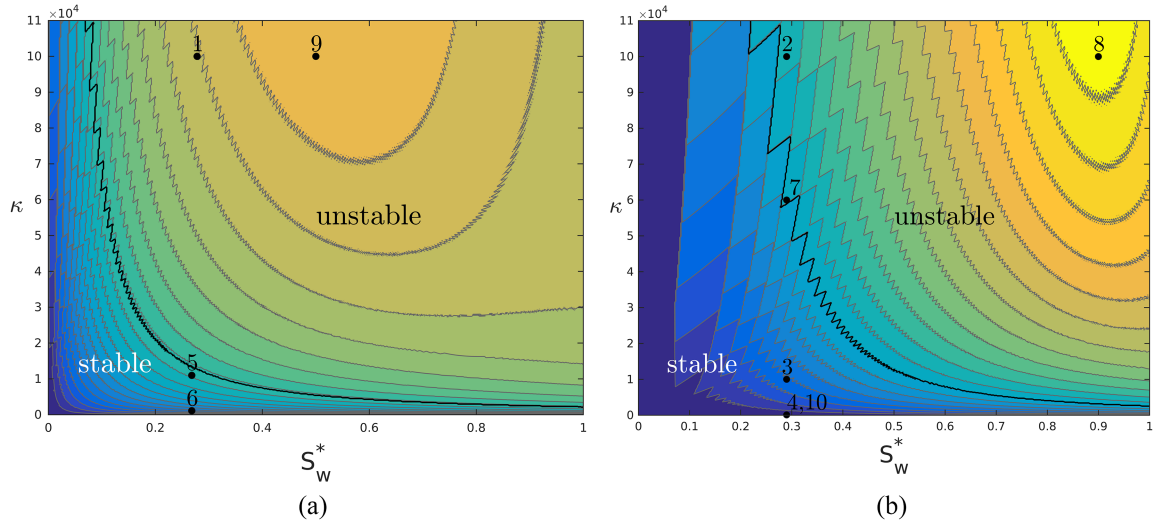


FIG. 8. Stability regions in the S_w^* - κ plane for the rest of the parameter set of (a) test case one and (b) test case two of Farajzadeh *et al.*¹⁰ The stable and unstable regions are separated by the thick black lines, and the different test cases are denoted by thick black dots.

Hence, strong foam (higher R with a small transition width κ) is usually stable, while weak foam (lower R) can become unstable quickly for relatively low values of κ . Test cases 1 and 2 are examples of weak foam and strong foam that are unstable, while test cases 3, 4, and 5 are stable according to this analysis. Finally we see that between the region of instability and stability there is a zone, which can be both stable and unstable. This is due to a strong sensitivity of the shock mobility, to the foam parameters κ and R , which becomes larger if R increases. Overall, we can deduce that the isolines of the dimensionless growth number are linear and hence we can write

$$\frac{\partial \Lambda}{\partial R} + a \frac{\partial \Lambda}{\partial \kappa} = 0, \quad (24)$$

where $a = \frac{\Delta \kappa}{\Delta R}$ is a constant wave propagation speed, which can be linked to the growth of disturbances in the κ - R space. This speed is highest for low R and high κ values.

The influence of the limiting water saturation S_w^* is more complicated, as can be seen in Figs. 8 and 9. These figures depict the disturbance velocity and show that the solutions are stable only for low values of the limiting water saturation. This can be partly explained by Fig. 5(a), which shows that the region where foam can exist for this model is limited to values of $S_w^* < 0.4$. Hence, a limiting water saturation that is larger implies that there is no foam present such that instabilities at the front are not subdued. Moreover, we observe that the region of the highest disturbance velocities is located around $S_w^* = 0.6$ for the first parameter set and around $S_w^* = 0.9$ for the second parameter set. As can be deduced from Fig. 7, the growth number is highest for low R and high κ . So, even if there is no foam present, the choice of S_w^* influences the stability of the solutions, since both the shock saturation and the shock velocity increase with an increasing limiting water saturation (see Fig. 5). The disturbance velocity scales linearly with the shock velocity and hence will increase too, and the

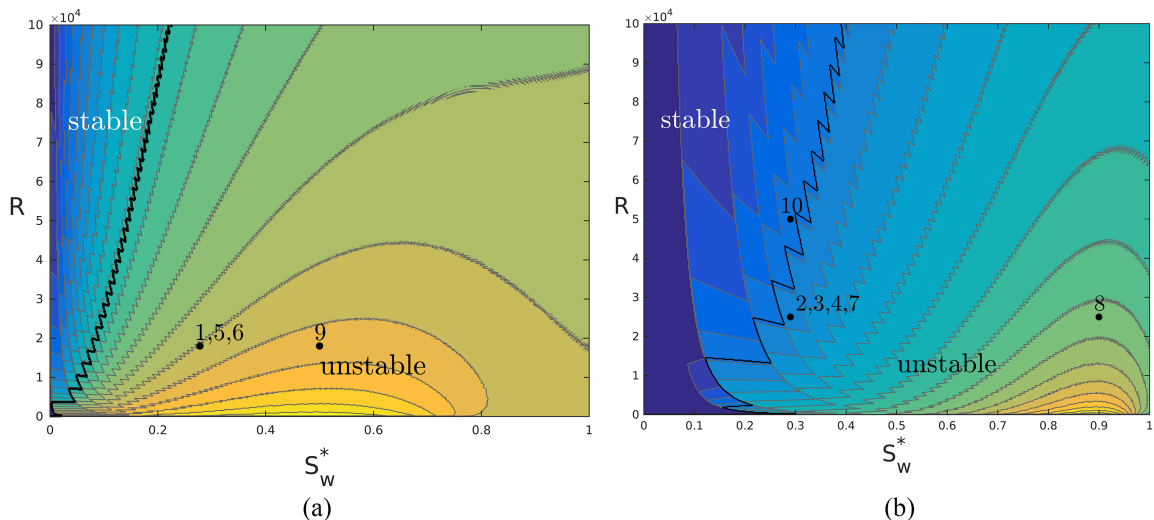


FIG. 9. Stability regions in the S_w^* - R plane for the rest of the parameter set of (a) test case one and (b) test case two of Farajzadeh *et al.*¹⁰ The stable and unstable regions are separated by the thick black lines, and the different test cases are denoted by thick black dots.

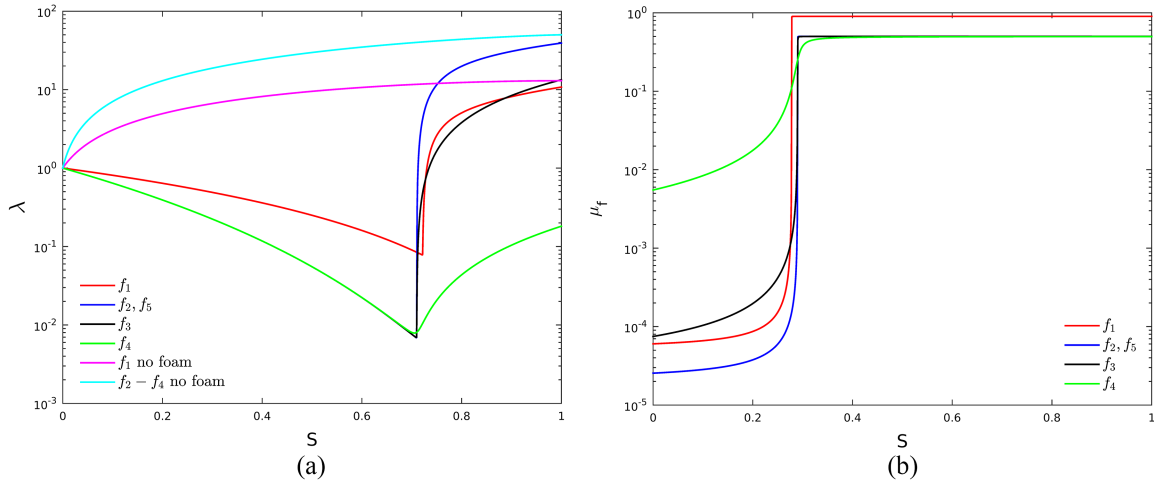


FIG. 10. (a) Total mobility and (b) apparent viscosity of the five test cases of Ref. 10.

dimensionless growth number depends on the mobility ratio around the shock, which will be larger if the shock saturation increases. Hence, we see that large values of S_w^* introduce a non-physical effect in the model by changing the shock saturation, although foam is absent. However, foams effective in surfactant-alternating-gas (SAG) applications are expected to have a small limiting water saturation in combination with a non-zero transition width.⁴

The online version of this article contains [supplementary material](#) where we introduce six additional test cases that are located in highly unstable or stable parts of the parameter space or around the boundaries of the stable parameter range. Those are also depicted in Figs. 7–9 and support the conclusions that can be drawn from this linear stability analysis.

V. NUMERICAL METHODS

The results from the linear stability analysis can be compared with the results obtained by high resolution two-dimensional numerical simulations of foam on a rectilinear grid with a horizontal injection well. The two-dimensional reservoir simulator was further developed by the first author for this purpose and based on the numerical simulator described in the study of Van der Meer *et al.*²⁶ We address the same test cases as in the study of Farajzadeh *et al.*¹⁰ For the second case, an interesting artifact was observed in the apparent viscosity of the foam, in the form of a fingering pattern behind the foam front (Fig. 6 in Ref. 10). These fingers did not significantly influence the saturation behind the front. Therefore, it was not clear from these results whether this is a physical effect or a numerical artifact. To analyze this effect and validate the numerical simulations of the foam model, we repeat the first four test cases of Farajzadeh *et al.*¹⁰

Instead of solving the equations in a fully implicit way, we opt for the implicit pressure explicit saturation (IMPES) method, which is designed for this kind of hyperbolic-elliptic problem because it takes into account the different nature of the equations. Because of the non-linearity in the foam parameters, the numerical stability of the foam simulations is a major concern.²⁵ To improve the stability of the numerical scheme,

a Taylor-Galerkin method is applied to the entire system. The non-linearity is accounted for by introducing auxiliary variables.¹ Using this scheme, we are able to resolve the very fast wave speeds that emerge from the non-linearity of the model. Additionally, solving the saturation equation explicitly with a higher-order scheme introduces less artificial diffusion. This is important in this case because we are interested in the detailed fingering behavior at the front and behind the front. By using operator splitting, as described in the study of Hvistendahl Karlsen *et al.*¹¹ and Van der Meer *et al.*,²⁶ we can split the saturation equation into a hyperbolic conservation law and an ordinary differential equation (ODE) for the mass flow rate. They are solved sequentially using a second-order Strang splitting scheme, which preserves the symmetry of the operator. The hyperbolic equation is solved with a second-order MUSCL scheme, which is a total variation diminishing finite volume method reconstructed from the first-order Godunov's method.²⁴ The Total Variation Diminishing (TVD) property prevents instabilities to occur that are due to the numerical method. In other words, a TVD scheme is monotonicity preserving if the Courant-Friedrichs-Levy (CFL) condition on the time step is satisfied.²⁴ The ODE is solved by the second-order trapezoidal rule, which is A-stable and therefore suitable for stiff ODEs.⁷ The size of the time step of an A-stable method does not suffer from stringent restrictions, and the choice only depends on the desired accuracy. For the elliptic equation (2), we use a multi-grid linear solver that combines a five-point stencil with a nine-point stencil that is rotated by 45° to reduce the grid-orientation effect.²⁷ The five-point stencil accounts for the unrotated coefficients and is combined with a nine-point stencil that accounts for the rotated coefficients and is projected back onto the original grid. The domain is parallelized by Message Passing Interface (MPI) using the HYPRE library⁸ to speed up the computations, since roughly 73% of the simulation time is spent on the pressure solver for this model.²⁸

VI. NUMERICAL RESULTS

The foam displacement is modeled in a reservoir of size $1 \times 1 \times 1$ m, discretized using 300 grid blocks in the first

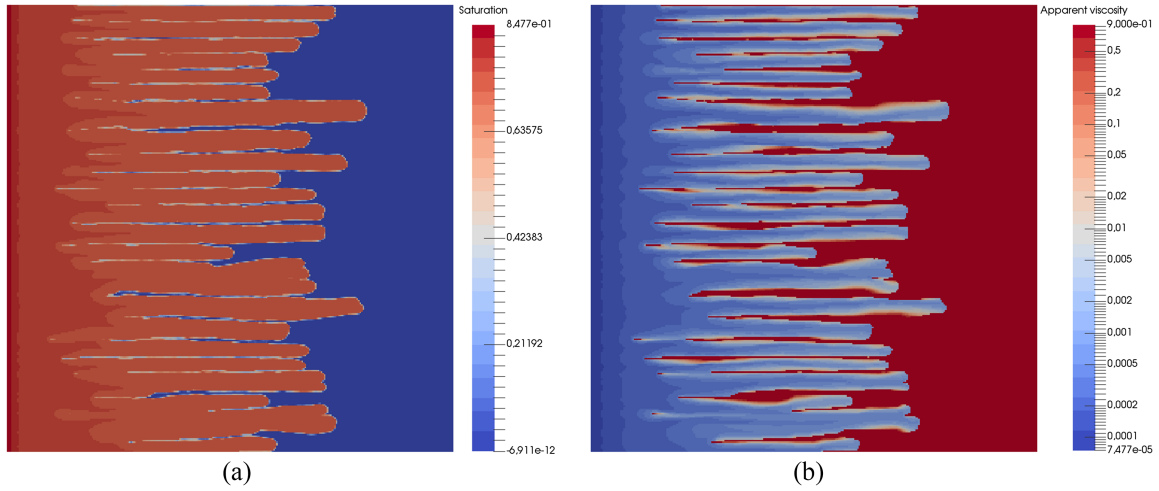


FIG. 11. (a) Saturation profile and (b) logarithm of the apparent foam viscosity, for the first test case of Ref. 10 after 0.4 PV of injected gas.

two directions and one grid block in the z -direction (hence we have a 2D model). The porous medium used in the model has porosity $\psi = 0.2$, and a log-random permeability field with an average permeability $K = 5 \times 10^{-13} \text{ m}^2$, a Dykstra-Parsons coefficient of 0.1, and correlation lengths $L_x = 0.01$ and $L_y = 0.01$. Initially the reservoir is filled with water mixed with surfactants, and pure gas is injected at a fixed injection rate I , via a horizontal injector along the entire left side of the reservoir. Water and gas are then produced via a horizontal producer along the right side of the reservoir, keeping the pressure constant at 50 bars. In Table I, the parameter values for each of the cases are specified. The resulting saturation and apparent viscosity profiles for the first four test cases and two reference cases are discussed later.

The apparent gas viscosity is given by the product of the gas viscosity and the mobility reduction factor,

$$\mu_f = \mu_g \cdot f_{mr}(S), \quad (25)$$

and is therefore a function of the saturation. This quantity will be greatest at the foam front and decrease quickly up to the injection point as shown in Fig. 10(b).

A. Test case 1

Test case 1 describes a foam displacement process with a relatively low resistance of foam to flow (R), and a low limiting water saturation (S_w^*), which means that the effective foam viscosity μ_f is still much higher than the water viscosity μ_w . Hence the flow is characterized by instabilities like viscous fingering, as shown in Fig. 11. This is reflected in the interfacial length, growth rate, and vorticity norm of the simulation (see Fig. 17). These consist of three stadia: first, there is a quick increase visible in the growth rate, thereafter it is more or less linear, and then it becomes constant.

B. Test case 2

The second test case describes strong foam, with a high resistance of foam to flow and high limiting water saturation, and a very sharp transition from gas to foam (κ). This sharp transition from gas to foam could potentially lead to numerical instability, if not treated with appropriate care.^{21,25} It was for this test case that¹⁰ observed the viscous fingering pattern behind the front in the apparent viscosity of the foam (see Fig. 12).

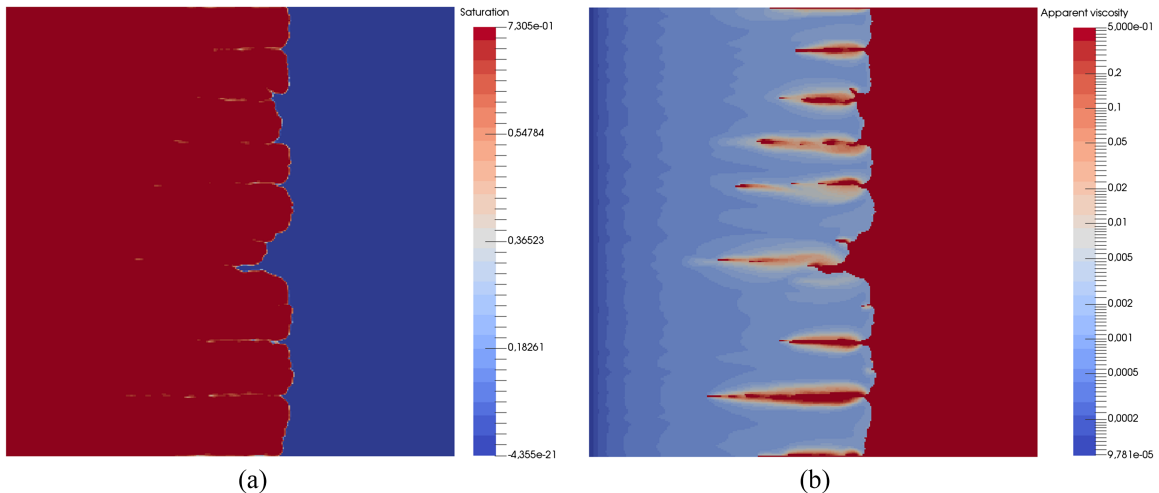


FIG. 12. (a) Saturation profile and (b) logarithm of the apparent foam viscosity, for the second test case of Ref. 10 after 0.35 PV of injected gas.

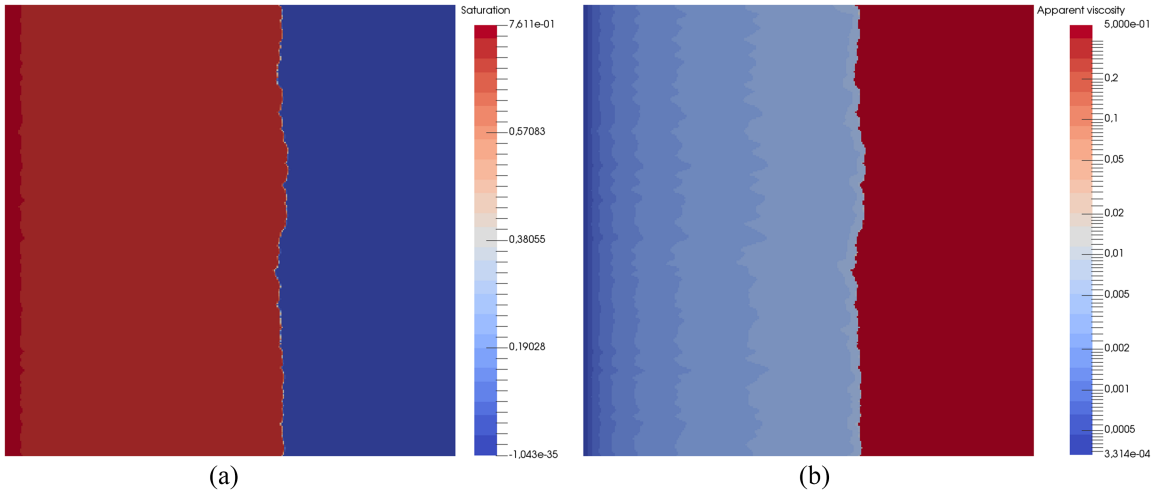


FIG. 13. (a) Saturation profile and (b) logarithm of the apparent foam viscosity, for the third test case of Ref. 10 after 0.42 PV of injected gas.

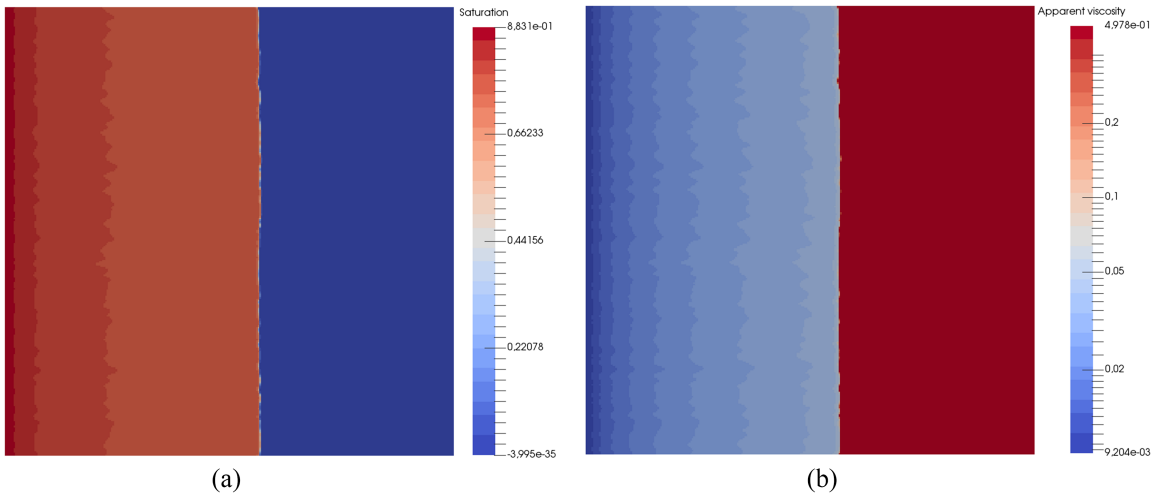


FIG. 14. (a) Saturation profile and (b) logarithm of the apparent foam viscosity, for the fourth test case of Ref. 10 after 0.42 PV of injected gas.

C. Test case 3

The third test case resembles test cases 2 and 4, apart from the transition speed from gas to foam, which is a factor 10 lower here than for test case 2 and a factor 10 higher than test case 4. The simulation results are shown in Fig. 13.

D. Test case 4

Test case 4 simulates strong foam, with a relatively wide transition zone between gas and foam. This means that the numerical method will have no major stability issues, and the restriction on the time step is less than for the three preceding cases. As shown in Fig. 14, the foam front is stable, since the foam is strong and no fingering behind the front is observed, which is in agreement with the results of Ref. 10.

E. Reference cases without foam

As a reference, we repeat the above simulations without foam for test cases 1 and 2 (cases 3 and 4 only differ in foam transition width from case 2). The simulation results are shown

in Figs. 15 and 16. Since there is no foam present, the apparent foam viscosity is equal to the gas viscosity, which is constant everywhere. Therefore, we show the total viscosity in the figures on the right. The difference in the solutions with foam is striking, since the fingers for these two cases are less pronounced, because the shock is much more diffused. Also, gas breakthrough is almost immediate for these cases, and the difference between cases 1 and 2 without foam is much less, than in the presence of foam.

VII. NUMERICAL STABILITY ANALYSIS

We can approximate the growth rate σ numerically,¹⁶ by the vorticity norm

$$\bar{\omega} = \sqrt{\int_0^1 \int_0^1 \omega^2 dx dy}, \quad (26)$$

where

$$\omega = \frac{1}{\lambda_T} \frac{d\lambda_T}{dS} \nabla S \times u, \quad (27)$$

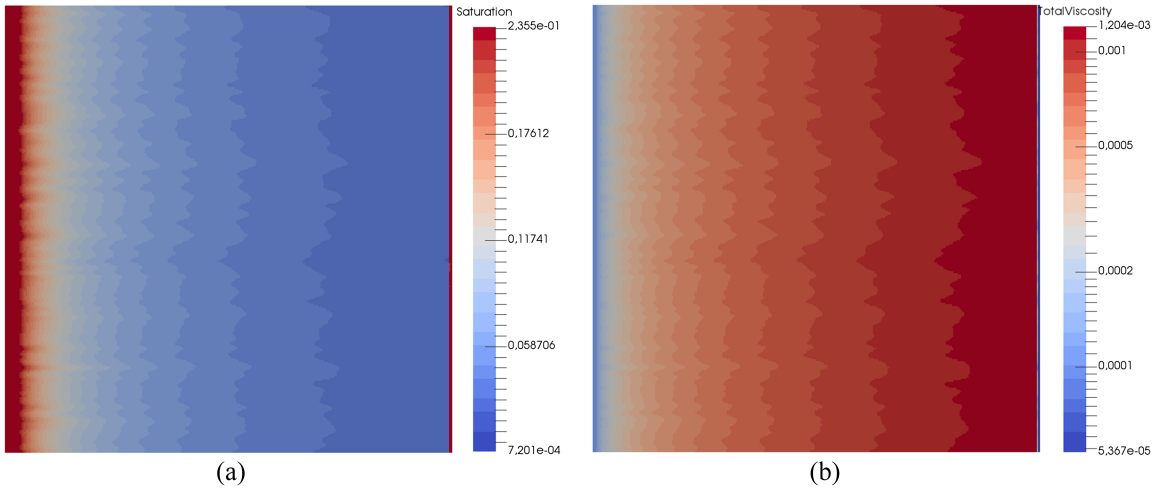


FIG. 15. (a) Saturation profile and (b) total viscosity, for simulation case 1 without foam after 0.12 PV of injected gas.

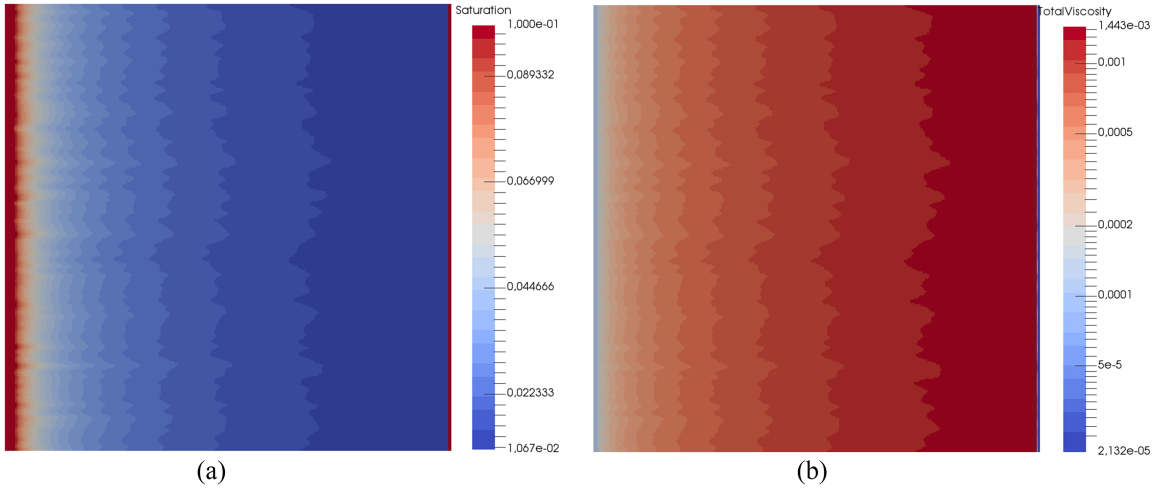


FIG. 16. (a) Saturation profile and (b) total viscosity, for simulation case 2 without foam after 0.06 PV of injected gas.

is a measure of the rotation at the finger tips. The maximum growth rate can then be approximated by

$$\sigma_{\max} \approx \ln\left(\frac{\bar{\omega}(t)}{\bar{\omega}(t - \Delta t)}\right) / \Delta t. \quad (28)$$

The dominant mode can be measured numerically as a function of time, using the energy spectrum of the solutions, so that

$$n_{\max} \approx \frac{\int_0^K kE(k, t) dk}{\int_0^K E(k, t) dk}, \quad (29)$$

where E is the energy spectrum,¹⁸ which is computed by

$$E(k, t) = \left(\int_0^1 \left[\int_0^1 \omega(x, y, t) dx \right] e^{-ikt} dy \right)^2. \quad (30)$$

The disturbance number Λ_{num} , which is a measure of perturbation growth with respect to the front speed, can then be approximated by

$$\Lambda_{\text{num}} = \frac{\sigma_{\max}}{n_{\max}}. \quad (31)$$

Likewise, the interfacial length Γ , which is a measure of the amount of fingering or instability going on, can be approximated numerically¹⁶ by

$$\Gamma \approx \int_0^1 \int_0^1 \sqrt{\left(\frac{\partial S}{\partial x}\right)^2 + \left(\frac{\partial S}{\partial y}\right)^2} dx dy. \quad (32)$$

In the figures below, those quantities were approximated for the same test cases as earlier (see Figs. 17–20) and compared to each other in Fig. 21. In Fig. 17, we see that the interfacial length shows three stages: starting off very fast for small times, and then very slowly descending, while finally becoming almost constant. Compared to the case without foam, the initial growth is larger, but while the no-foam case slows down eventually due to merging of small fingers into big ones,^{17,29} the interfacial length for this weak foam case keeps increasing over the observed period of time. It could be the case that a larger reservoir is needed for the interfacial length to decrease. Also we have to mention that the approximated interfacial length sums over the squared partial derivatives in each grid block. Since the foam model contains a peak in the derivative

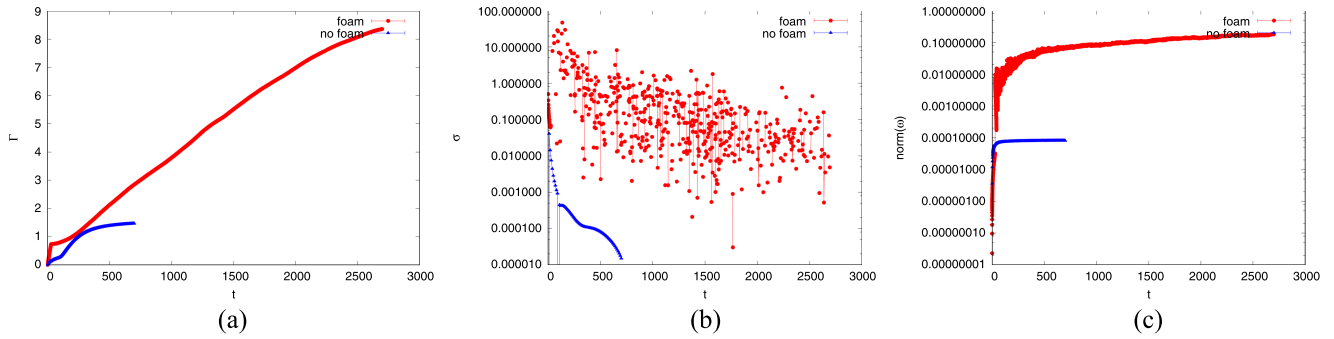


FIG. 17. Numerical approximation of the interfacial length, growth rate, and vorticity norm for test case 1 of Farajzadeh *et al.*¹⁰ (a) Interfacial length, (b) growth rate, (c) vorticity norm.

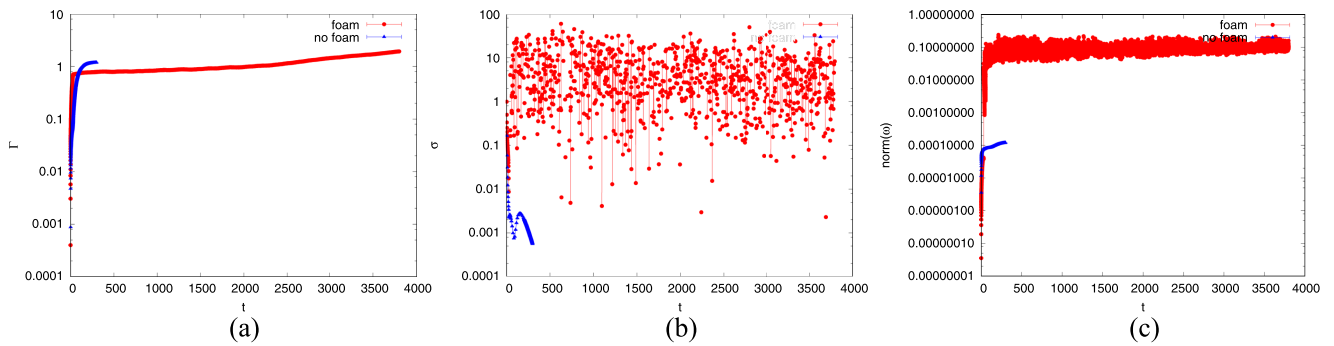


FIG. 18. Numerical approximation of the interfacial length, growth rate, and vorticity norm for test case 2 of Farajzadeh *et al.*¹⁰ (a) Interfacial length, (b) growth rate, (c) vorticity norm.

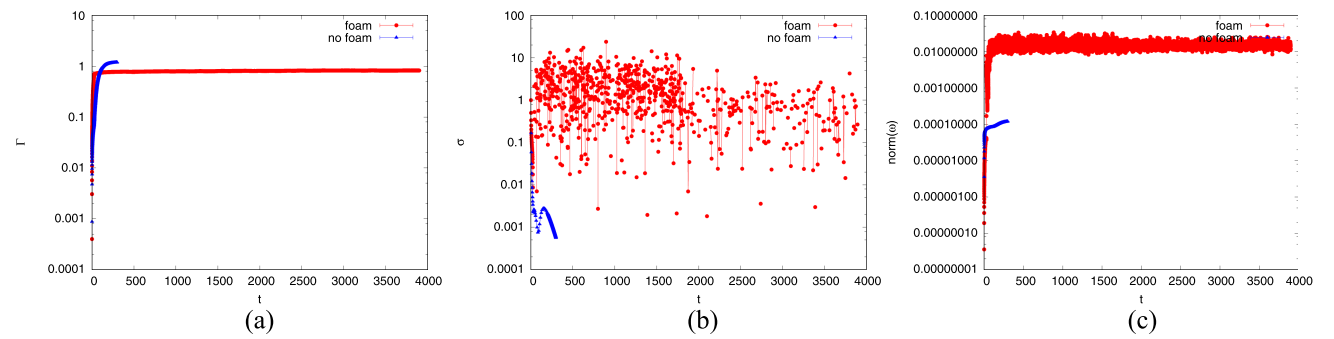


FIG. 19. Numerical approximation of the interfacial length, growth rate, and vorticity norm for test case 3 of Farajzadeh *et al.*¹⁰ (a) Interfacial length, (b) growth rate, (c) vorticity norm.

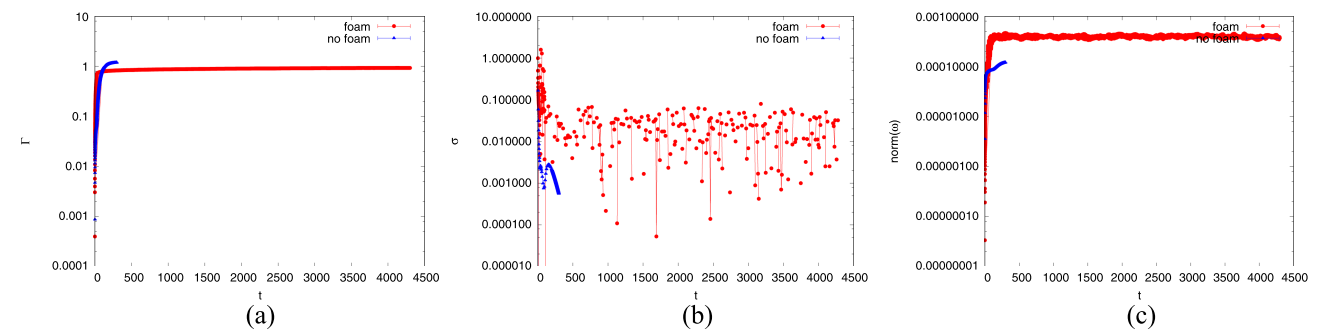


FIG. 20. Numerical approximation of the interfacial length, growth rate, and vorticity norm for test case 4 of Farajzadeh *et al.*¹⁰ (a) Interfacial length, (b) growth rate, (c) vorticity norm.

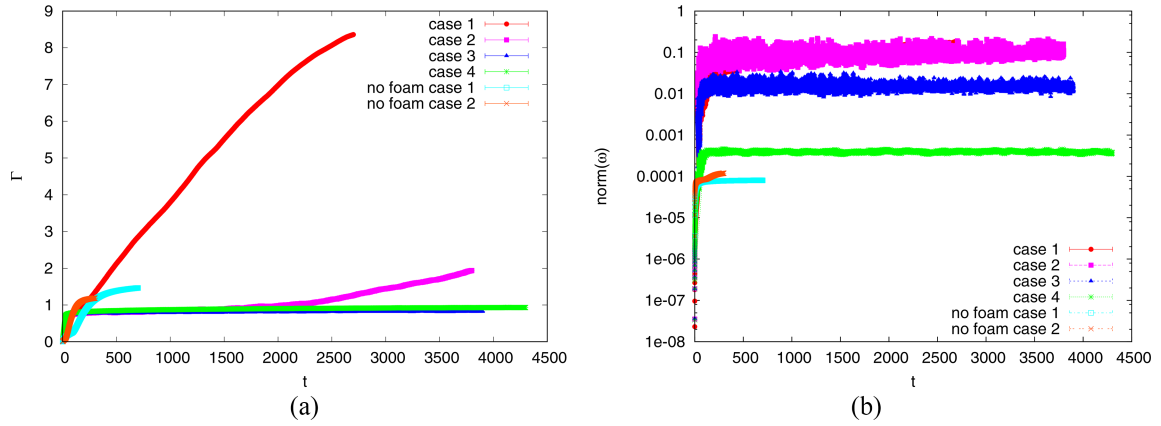


FIG. 21. Numerical approximation of the interfacial length and vorticity norm for the first four test cases of Farajzadeh *et al.*¹⁰ (a) Interfacial length, (b) vorticity norm.

around the limiting water saturation, this approximation overestimates the total interfacial length at the front. This measure is therefore more suited to compare the quantitative behavior of the fingers with each other, than to give a qualitative measure for the front interfacial length. The same is true for the growth rate, which takes into account the derivative of the mobility, which is highest behind the front, and thus does not directly reflect the instabilities at the front. However, it was the unstable behavior behind the front that is of interest in this paper. The consequence of this is that the growth rate of instability measure shows a much higher variation than for the foam case. The average growth rate is more or less constant after an initial increase. The growth rate for the case without foam is decreasing first and later showing a small increase that could be due to numerical issues since it was not observed by Riaz and Tchelepi.¹⁶ The vorticity norm gives a more consistent pattern, which resembles the interfacial length, and after a fast initial growth, shows a slight decrease after which it increases very slowly.

For the second test case, we see the same initial increase of the interfacial length as for the first test case in Fig. 18, after which it remains constant. The same case without foam shows a gradual increase which becomes constant after some time. The growth rate decreases for the model without foam after which it becomes negative (due to the gas reaching the right boundary). For the strong-foam model, we see again a huge variation in the growth rate, and the vorticity norm shows a steep increase after which it becomes constant. Again, the vorticity norm is higher than for the case without foam, due to the large derivatives of the mobility behind the front.

Test case 3, depicted in Fig. 19, gives results almost identical to the second test case, but an order 10 smaller for the growth rate and the interfacial length. The same holds for the fourth test case in Fig. 20, in which the growth rate is reduced by an order 1000 with respect to test case 2. Hence, we can assume that the vorticity norm of the simulations depends linearly on the parameter κ , for a strong foam (test case 2, 3, and 4), i.e.,

$$\bar{\omega} \sim \kappa. \quad (33)$$

This means that reducing κ by approximately a factor 10 leads to a reduction in the vorticity norm by a factor 10. This can

also be seen in Fig. 21, where the test cases are compared to each other. However, it shows that the vorticity of test case 1 is an order 10 lower than of test case 2, although they have the same transition width. This can be due to a lower mobility reduction factor for test case 1 (see Table I), which causes a smaller mobility derivative around the limiting water saturation. Hence a lower vorticity is expected behind the front, whereas an increase in fingering at the front should partly compensate for this. The interfacial length is largest for the cases without foam (until the front in the second case reaches the right side of domain, and the interfacial length drops below that of the first foam case). After that, weak foam shows the highest interfacial length, as we could also observe from the saturation plots. The strong-foam cases are all really stable at the front and therefore more or less constant around the same value. On the other hand, the average growth rate for test case 2 is almost as large as for test case 1, which implies that instabilities behind the front must contribute to this result. The average growth rate of the other two test cases are smaller and almost zero. The growth rate of the case without foam is not comparable here because of the chosen measure, as was explained before. If we compare the results with the linear stability analysis, we see that indeed a higher non-linearity (i.e., a smaller transition width from gas to foam) leads to more instability.

VIII. CONCLUSIONS

The physical instabilities that were observed behind the front in the study of Farajzadeh *et al.*¹⁰ seem to be inherent to the non-linearity in the mobility of foam. The linear stability analysis made it clear that the foam parameters κ , R , and S_w^* had a significant influence on the physical stability of the results. We could identify stability regions in the foam parameter space by calculating the dimensionless disturbance number, which show for which parameter sets the solutions are potentially stable or unstable. The first four test cases studied in this paper, and the additional test cases that are available in the [supplementary material](#), confirmed these results numerically.

We found that strong foam with a narrow transition width between gas and foam (test case 2) shows the highest growth rate of all test cases, although the front is most stable. We

investigated the influence of the parameters that determine foam strength, transition width, and critical water saturation on the stability characteristics of the solutions. It shows that a high mobility reduction factor (foam strength) has a stabilizing effect on the solutions, while a higher non-linearity of the gas-foam transition (shorter transition width) has a destabilizing effect. It turns out that the growth rate of instabilities is linearly dependent on both the inverse foam strength and transition width control parameters ($1/R$ and κ). There is also a strong effect of the critical water saturation on the stability characteristics.

In this research, we neglected the influence of capillarity in both the linear stability analysis and the simulations because it has a damping effect on the instabilities at the front. For a more realistic outcome, the effect of additional diffusion could be investigated. Furthermore, we could extend this analysis to a quarter-five spot setup. This would add an extra complexity to the model due to a spatially varying strain field that affects the stability front, as was shown for a miscible flow case in the study of Chen and Meiburg.⁶ Moreover, we recommend to extend the current local equilibrium foam models to more complex models at the front to gain more insight into the nature of instabilities that occur behind the foam front and to investigate whether they are able to cause an unstable displacement. In this case models that take into account the gas-foam interface might give an outcome.

In this paper, we did not compare our stability or numerical results with experimental results, since those experiments do not exist for this particular study. Experiments that look at fingering phenomena of a highly mobile gas being injected into the low-mobile foam would be very valuable to validate numerical simulations of foam enhanced oil recovery processes. One way to do this would be to create foam between two glass plates with obstacles in between, to mimic the porous rock in two dimensions. After this gas could be injected through a hole into the middle of the plates, in order to study the fingering behavior in a porous medium in the presence of foam. These results can then be compared to highly accurate simulations in two dimensions.

Finally the results from the stability analysis can be used to identify important scales and wavelengths of the problem, which in turn can be adapted in building an efficient numerical solver that is able to capture both the fast waves that occur due to the foam and the slow waves occurring in the rarefaction wave.

SUPPLEMENTARY MATERIAL

See [supplementary material](#) for the additional six test cases that are located in highly unstable or stable parts of the foam parameter space or around the boundaries of the stable parameter range.

ACKNOWLEDGMENTS

This research was carried out within the context of the Recovery Factory project at Delft University of Technology (TU Delft), sponsored by Shell Global Solutions International. We would like to thank Dr. Hajibeygi of TU Delft for useful

discussions and suggestions about the stability analysis of the foam model.

APPENDIX A: DERIVATION OF THE TWO-PHASE FLOW EQUATIONS

In subsections 1 and 2 of Appendix A, we give a derivation of the non-dimensional incompressible, immiscible two-phase flow equations for gas and water and foam in a porous medium. Mass conservation of each phase, which is described by a mass-balance equation for the phase saturation $S_\alpha \in [0, 1]$, is given by

$$\phi \partial_t S_\alpha = -\nabla \cdot \mathbf{u}_\alpha, \quad (\text{A1})$$

where the subscript $\alpha \in \{w, g, f\}$ denotes the phase (water, gas, or foam in this case), ϕ denotes the reservoir porosity, and \mathbf{u}_α denotes the phase velocity that is given by

$$\mathbf{u}_\alpha = -\lambda_\alpha (\nabla P_\alpha + \rho_\alpha \mathbf{g}). \quad (\text{A2})$$

Here P_α is the phase pressure, ρ_α is the phase density, \mathbf{g} is the gravitational force, and λ_α is the phase mobility,

$$\lambda_\alpha = k \frac{k_{r\alpha}(S_\alpha)}{\mu_\alpha}, \quad (\text{A3})$$

where k is the absolute permeability, μ_α is the phase viscosity, and $k_{r\alpha}$ is the phase relative permeability, which is defined in the main part of this article.

1. Two-phase flow

In case of two fluids, the difference between the phase pressures is described by the capillary pressure, defined as

$$P_c \equiv P_w - P_g, \quad (\text{A4})$$

such that

$$\mathbf{u}_w = -\lambda_w (\nabla P_c + \nabla P_g + \rho_w \mathbf{g}), \quad (\text{A5})$$

$$\mathbf{u}_g = -\lambda_g (\nabla P_g + \rho_g \mathbf{g}). \quad (\text{A6})$$

The total velocity, which is the sum of the phase velocities, is thus equal to

$$\mathbf{u} = -\left[\lambda_T \nabla P_g + \lambda_w \nabla P_c + (\lambda_w \rho_w + \lambda_g \rho_g) \mathbf{g} \right], \quad (\text{A7})$$

where λ_T is the total mobility (sum of mobilities). Hence, we can express the phase velocity of water in terms of the total velocity as follows:

$$\begin{aligned} \mathbf{u}_w &= -\lambda_w \nabla P_c + \frac{\lambda_w}{\lambda_T} (\mathbf{u} + \lambda_w \nabla P_c + \lambda_g (\rho_g - \rho_w) \mathbf{g}) \\ &= \frac{\lambda_w}{\lambda_T} \mathbf{u} - \frac{\lambda_w \lambda_g}{\lambda_T} (\nabla P_c + \Delta \rho \mathbf{g}) \\ &= f_w \mathbf{u} - \lambda_w f_g (\nabla P_c + \Delta \rho \mathbf{g}), \end{aligned} \quad (\text{A8})$$

where $f_\alpha = \lambda_\alpha / \lambda_T$ is the phase fractional flow function and $\Delta \rho = \rho_w - \rho_g$. Hence we can express Eq. (1) as

$$\phi \partial_t S_w = -\nabla \cdot f_w (\mathbf{u} - \lambda_g (P'_c \nabla S_w + \Delta \rho \mathbf{g})), \quad (\text{A9})$$

where P'_c is the derivative of the capillary pressure with respect to the phase saturation,¹⁶ that is approximated by

$$P'_c = \sqrt{\frac{\phi}{k}} \gamma_{gw} \sin(\theta), \quad (\text{A10})$$

where γ_{gw} is the interfacial tension between gas and water and θ is the tilting angle of the rectangular domain with respect to the gravitational force. From the definition of saturation, it follows that the sum of the phase saturations is one everywhere, i.e.,

$$\sum_{\alpha} S_{\alpha} = 1, \text{ with } \alpha \in \{w, g\}, \quad (\text{A11})$$

so that we only have to solve for one phase. Hence, Eqs. (10), (11), and (13) imply that

$$\nabla \cdot \mathbf{u} = 0, \quad (\text{A12})$$

which describes the pressure decay in the porous medium.

2. Non-dimensional formulation

To reduce the number of parameters, we scale the model given by Eqs. (1), (2), and (14), in a similar way as was done by Riaz and Tchelepi.¹⁶ If we let U be a characteristic velocity scale, L be a characteristic length scale of the model, and W be a characteristic width scale, such that $A = L/W$ is the aspect ratio, we can scale the other variables as follows:

$$x = L\tilde{x}, \quad (\text{A13})$$

$$y = W\tilde{y}, \quad (\text{A14})$$

$$\nabla = \frac{\tilde{\nabla}}{L}, \quad (\text{A15})$$

$$\mathbf{u} = U\tilde{\mathbf{u}}, \quad (\text{A16})$$

$$t = \frac{\phi L(1 - S_{wc} - S_{gr})}{U} \tilde{t}, \quad (\text{A17})$$

$$P = \frac{\mu UL}{k} \tilde{P}, \quad (\text{A18})$$

$$P'_c = \gamma_{gw} \sqrt{\frac{\phi}{k}} \tilde{P}'_c, \quad (\text{A19})$$

where the tilde denotes a non-dimensional variable. The relative permeability functions are scaled by their end point relative permeabilities, i.e., the relative permeability of the residual water and gas saturation, $k_{rwe} = k_{rw}(S_{gr})$ and $k_{rge} = k_{rg}(1 - S_{wc})$, respectively. The gas saturation is normalized by $\tilde{S}_g = \frac{(S_g - S_{gr})}{(1 - S_{wc} - S_{gr})}$. Substituting these variables into the two-dimensional model leads to a non-dimensional system of the form

$$\partial_{\tilde{t}} \tilde{S}_g = -\tilde{\nabla} \cdot \left[M \frac{\tilde{k}_{rg}}{\tilde{\lambda}} \left(\tilde{\mathbf{u}} - \frac{\tilde{k}_{rw}}{N_{ca}} \tilde{P}'_c \tilde{\nabla} \tilde{S}_g - \tilde{k}_{rw} \frac{G}{M} \tilde{\nabla} z \right) \right], \quad (\text{A20})$$

$$\tilde{\mathbf{u}} = -\tilde{\lambda}_w \tilde{\nabla} \tilde{P}_c - \tilde{\lambda} \tilde{\nabla} \tilde{P}_g - \lambda_w G \tilde{\nabla} z, \quad (\text{A21})$$

$$\tilde{\nabla} \tilde{\mathbf{u}} = 0, \quad (\text{A22})$$

where $\tilde{\lambda} = M \tilde{k}_{rg} + \tilde{k}_{rw}$ is the dimensionless mobility function. Here, the variables M , G , and N_{ca} denote the end point mobility ratio, gravity number, and capillary number, respectively, which are given by

$$M = \frac{\mu_w k_{rge}}{\mu_g k_{rwe}}, \quad (\text{A23})$$

$$G = \frac{k \Delta \rho g}{\mu_g U}, \quad (\text{A24})$$

$$N_{ca} = \frac{U \mu_w}{\gamma_{gw} \sin(\theta)}, \quad (\text{A25})$$

where g is the magnitude of the gravitational force. The mobility ratio together with the dimensionless foam parameters R , κ , and S_w^* , the dimensionless injection rate \tilde{I} , and the porosity ϕ determines the entire behavior of the fluids for a certain initial boundary value problem. In the rest of the article, we will drop the tilde for readability and define $S \equiv S_g$ and $f \equiv \frac{k_{rg} M}{\lambda}$.

APPENDIX B: DERIVATION OF THE PERTURBATION EQUATIONS

Here we derive the equations used for the stability analysis that is described in the study of Riaz and Tchelepi.¹⁹ For this, we rewrite Eqs. (1) and (2) in terms of the transformed variable $\xi = x - v_s t$, y , and t , so that

$$\partial_t S - v_s \partial_{\xi} S + \nabla \cdot (k_{rw} \nabla \bar{P}) = 0, \quad (\text{B1})$$

$$\nabla \cdot \left(\lambda \nabla \bar{P} - G k_{rg} \nabla z - \frac{k_{rg}}{Ca} P'_c \nabla S \right) = 0. \quad (\text{B2})$$

Substituting $(S, P)(\xi, y, t) = (S_0, P_0)(\xi) + (\hat{s}, \hat{p})(\xi) e^{iny + \sigma t}$ in Eq. (1) gives

$$\partial_t S - v_s \partial_{\xi} S + \partial_{xi}(k_{rw} \partial_{xi} \bar{P}) + \partial_y(k_{rw} \partial_y \bar{P}) = 0, \quad (\text{B3})$$

and hence

$$\partial_t S + \partial_{\xi} (k_{rw} \partial_{\xi} \bar{P} - v_s S) + k_{rw} \partial_{yy} \bar{P} + k'_{rw} \partial_y S \partial_y \bar{P} = 0. \quad (\text{B4})$$

Evaluating all derivatives to y and t leads to

$$\begin{aligned} \sigma \hat{s} e^{iny + \sigma t} + \partial_{\xi} (k_{rw} (P'_0 + \hat{p}' e^{iny + \sigma t}) - v_s (S_0 + \hat{s} e^{iny + \sigma t})) \\ = n^2 k_{rw} \hat{p} e^{iny + \sigma t} + n^2 k'_{rw} \hat{p} (e^{iny + \sigma t})^2. \end{aligned} \quad (\text{B5})$$

Multiplying the equation with $e^{-(iny + \sigma t)}$ gives

$$\begin{aligned} \sigma \hat{s} + \partial_{\xi} (k_{rw} P'_0 e^{-(iny + \sigma t)} + k_{rw} \hat{p}' - v_s S_0 e^{-(iny + \sigma t)} - v_s \hat{s}) \\ = n^2 k_{rw} \hat{p} + n^2 k'_{rw} \hat{p} e^{iny + \sigma t}. \end{aligned} \quad (\text{B6})$$

Now, we express $k_{rw}(S)$ in terms of S_0 by using a Taylor expansion, such that

$$\begin{aligned} k_{rw}(S) &= k_{rw}(S_0) + k'_{rw}(S_0)(S - S_0) + \mathcal{O}((\Delta S)^2) \\ &= k_{rw}(S_0) + k'_{rw}(S_0) \hat{s} e^{iny + \sigma t} + \mathcal{O}((\hat{s})^2). \end{aligned} \quad (\text{B7})$$

Substituting this in the above equation we obtain

$$\begin{aligned} \sigma \hat{s} + \partial_{\xi} (k_{rw}(S_0) P'_0 e^{-(iny + \sigma t)} + k'_{rw}(S_0) P'_0 \hat{s} + k_{rw}(S_0) \hat{p}' \\ + k'_{rw}(S_0) \hat{p} \hat{s}' e^{iny + \sigma t} - v_s S_0 e^{-(iny + \sigma t)} - v_s \hat{s}) \\ = n^2 k_{rw}(S_0) \hat{p} + n^2 k'_{rw}(S_0) \hat{p} e^{iny + \sigma t} \\ + n^2 k''_{rw}(S_0) \hat{s}^2 \hat{p} e^{2 \cdot (inx + \sigma t)} + \mathcal{O}((\hat{s})^2). \end{aligned} \quad (\text{B8})$$

Neglecting all the higher order terms that include $\hat{s} \hat{p}$, \hat{s}^2 , and $\hat{s} \hat{p}'$ and assuming that $e^{-(iny + \sigma t)} \rightarrow 0$ if $\sigma > 0$ and $t > 0$, we find that

$$\sigma \hat{s} + \partial_{\xi} (k_{rw}(S_0) \hat{p}' + (k'_{rw}(S_0) P'_0 - v_s) \hat{s}) = n^2 k_{rw}(S_0) \hat{p}. \quad (\text{B9})$$

We apply the same technique to Eq. (2), such that

$$\partial_\xi \left(\lambda \partial_\xi \bar{P} - Gk_{rg} - \frac{k_{rg}}{\text{Ca}} P'_c \partial_\xi S \right) = -\partial_y \left(\lambda \partial_y \bar{P} - \frac{k_{rg}}{\text{Ca}} P'_c \partial_y S \right), \quad (\text{B10})$$

so that

$$\begin{aligned} \partial_\xi \left(\lambda (P'_0 + \hat{p}') e^{iny+\sigma t} - Gk_{rg} - \frac{k_{rg}}{\text{Ca}} P'_c (S'_0 + \hat{s}') e^{iny+\sigma t} \right) \\ = n^2 \lambda \hat{p} e^{iny+\sigma t} - n^2 \frac{k_{rg}}{\text{Ca}} P'_c \hat{s} e^{iny+\sigma t}, \end{aligned} \quad (\text{B11})$$

and hence

$$\begin{aligned} \partial_\xi \left(\lambda (P'_0 e^{-(iny+\sigma t)} + \hat{p}') - Gk_{rg} e^{-(iny+\sigma t)} \right. \\ \left. - \frac{k_{rg}}{\text{Ca}} P'_c (S'_0 e^{-(iny+\sigma t)} + \hat{s}') \right) = n^2 \lambda \hat{p} - n^2 \frac{k_{rg}}{\text{Ca}} P'_c \hat{s}. \end{aligned} \quad (\text{B12})$$

We can express $\lambda(S)$, $k_{rg}(S)$, and $P'_c(S)$ in terms of S_0 with a second-order accurate Taylor expansion. Neglecting higher order terms, that contain multiples of \hat{s} and \hat{p} or \hat{p}' , and letting $e^{-(iny+\sigma t)} \rightarrow 0$ lead to

$$\begin{aligned} \partial_\xi \left(\lambda \hat{p}' + \left(\lambda' P'_0 - Gk'_{rg} - \frac{1}{\text{Ca}} (k_{rg} P'_c)' S'_0 \right) \hat{s} - \frac{k_{rg}}{\text{Ca}} P'_c \hat{s}' \right) \\ = n^2 \lambda \hat{p} - n^2 \frac{k_{rg}}{\text{Ca}} P'_c \hat{s}. \end{aligned} \quad (\text{B13})$$

Equations (9) and (13) described an eigenvalue problem with eigenvalue σ , in terms of the eigenfunctions \hat{s} and \hat{p} ,

$$\sigma \hat{s} + \partial_\xi \left(k_{rw} \hat{p}' + (k'_{rw} P'_0 - v_s) \hat{s} \right) = n^2 k_{rw} \hat{p}, \quad (\text{B14})$$

$$\begin{aligned} \partial_\xi \left(\lambda \hat{p}' + \left(\lambda' P'_0 - Gk'_{rg} - \frac{1}{\text{Ca}} (k_{rg} P'_c)' S'_0 \right) \hat{s} - \frac{k_{rg}}{\text{Ca}} P'_c \hat{s}' \right) \\ = n^2 \lambda \hat{p} - n^2 \frac{k_{rg}}{\text{Ca}} P'_c \hat{s}, \end{aligned} \quad (\text{B15})$$

where the functions k_{rw} , k_{rg} , and P_c are functions of S_0 and the apostrophe denotes the derivative with respect to S_0 or ξ , respectively. The base state functions S_0 and P_0 obey the boundary values of the Buckley-Leverett problem and obtain their maximum gradient at $\xi = 0$ and the eigenfunctions $(\hat{s}, \hat{p}) = 0$ and $(\hat{s}', \hat{p}') = 0$ at $\xi = \pm\infty$. This system can be solved numerically¹⁶ or by matched asymptotic expansions.¹⁹

In the absence of capillarity ($\text{Ca} \rightarrow \infty$), the base state satisfies

$$\frac{S_0}{d\xi} = \delta(\xi), \quad (\text{B16})$$

$$\frac{dP_0}{d\xi} = \frac{Gk_{rg} - 1}{\lambda}, \quad (\text{B17})$$

so that it follows from the interface and boundary conditions, that $\hat{s} = c_1 \delta(\xi)$, $\forall \xi \in (-\infty, \infty)$ and $c_1 \in \mathbb{R}$.¹⁹ Away from the discontinuity at $\xi = 0$, Eq. (14) implies that

$$\partial_\xi (k_{rw} \hat{p}') = n^2 k_{rw} \hat{p} \Rightarrow \hat{p}'' = n^2 \hat{p} \Rightarrow \hat{p} = ce^{\pm n\xi}. \quad (\text{B18})$$

Since $\hat{p} = \hat{p}' = 0$ at $\xi = \pm\infty$, it follows that

$$\hat{p}^{+0} = c_2 e^{-n\xi}, \quad \forall \xi > 0, c_2 \in \mathbb{R}, \quad (\text{B19})$$

$$\hat{p}^{-0} = c_3 e^{+n\xi}, \quad \forall \xi < 0, c_2 \in \mathbb{R}. \quad (\text{B20})$$

Integrating the full system with capillarity given by Eqs. (14) and (15) over the discontinuity (from 0^- to 0^+) gives us two equations in terms of p^{+0} , p^{-0} , and σ ,

$$k_{rw}(S_0(0^{+0})) \hat{p}'^{+0} - k_{rw}(S_0(0^{-0})) \hat{p}'^{-0} = -c_1 \sigma, \quad (\text{B21})$$

$$\lambda(S_0(0^{+0})) \hat{p}^{+0} - \lambda(S_0(0^{-0})) \hat{p}^{-0} = 0. \quad (\text{B22})$$

Evaluating the indefinite integral of Eq. (14) over ξ leads to

$$\hat{p}' + c_1 (\lambda' P_0 - Gk_{rg}) \delta(\xi) = c_4 / \lambda + n^2 \int \hat{p} d\xi. \quad (\text{B23})$$

Rewriting the terms between brackets as $-P''_0 / \delta(\xi)$ by differentiating Eq. (17) with respect to ξ gives

$$\hat{p}' - c_1 P''_0 = c_4 / \lambda + n^2 \int \hat{p} d\xi. \quad (\text{B24})$$

Integrating this expression over the discontinuity gives a third equation in terms of \hat{p}^{+0} and \hat{p}^{-0} ,

$$\hat{p}^{+0} - \hat{p}^{-0} = c_1 (P'^{+0}_0 - P'^{-0}_0). \quad (\text{B25})$$

Equations (21), (22), and (25) then lead to an expression for the disturbance velocity

$$\frac{\sigma}{n} = \frac{f_{g1} - f_{g0}}{S_1 - S_0} \frac{\lambda_1 (1 - Gk_{rg0}) - \lambda_0 (1 - Gk_{rg1})}{\lambda_1 - \lambda_0}, \quad (\text{B26})$$

where the subscripts 0 and 1 denote the front and back edges of the shock, respectively.

APPENDIX C: MODEL PARAMETERS

The parameter values and explanations of the four test cases that were introduced in Sec. IV are given in Table I.

- ¹Ambrosi, D. and Quartapelle, L., "A Taylor-Galerkin method for simulating nonlinear dispersive water waves," *J. Comput. Phys.* **146**(2), 546–569 (1998).
- ²Ashoori, E., Marchesin, D., and Rossen, W. R., "Roles of transient and local equilibrium foam behavior in porous media: Traveling wave," *Colloids Surf., A* **377**(1-3), 228–242 (2011).
- ³Ashoori, E., Marchesin, D., and Rossen, W. R., "Stability analysis of uniform equilibrium foam states for EOR processes," *Transp. Porous Media* **92**(3), 573–595 (2012).
- ⁴Boeije, C. S. and Rossen, W. R., "Fitting foam simulation model parameters for SAG foam applications," in *Proceedings of SPE Enhanced Oil Recovery Conference* (Society of Petroleum Engineers, 2013).
- ⁵Boeije, C. S. and Rossen, W. R., "Gas-injection rate needed for SAG foam processes to overcome gravity override," *SPE J.* **20**(01), 049–059 (2015).
- ⁶Chen, C.-Y. Y. and Meiburg, E. E., "Miscible porous media displacements in the quarter five-spot configuration. Part 2. Effect of heterogeneities," *J. Fluid Mech.* **371**, 269–299 (1998).
- ⁷Dahlquist, G. G., "A special stability problem for linear multistep methods," *BIT Numer. Math.* **3**(1), 27–43 (1963).
- ⁸Falgout, R. D. and Yang, U. M., "Hypre: A library of high performance preconditioners," *Lect. Notes. Comput. Sci.* **2331**, 632–641 (2002).
- ⁹Farajzadeh, R., Lotfollahi, M., Eftekhari, A., Rossen, W. R., and Hirasaki, G. J. H., "Effect of permeability on implicit-texture foam model parameters and the limiting capillary pressure," *Energy Fuels* **29**(5), 3011–3018 (2015).
- ¹⁰Farajzadeh, R., Eftekhari, A. A., Hajibeygi, H., Kahrobaei, S., van der Meer, J. M., Vincent-Bonnieu, S., and Rossen, W. R., "Simulation of instabilities and fingering in surfactant alternating gas (SAG) foam enhanced oil recovery," *J. Nat. Gas Sci. Eng.* **34**, 1191–1204 (2016).
- ¹¹Hvistendahl Karlsen, K., Lie, K. A., Natvig, J., Nordhaug, H., and Dahle, H., "Operator splitting methods for systems of convection-diffusion equations: Nonlinear error mechanisms and correction strategies," *J. Comput. Phys.* **173**(2), 636–663 (2001).

- ¹²Khatib, Z., Hirasaki, G., and Falls, A., “Effects of capillary pressure on coalescence and phase mobilities in foams flowing through porous media,” *SPE Reservoir Eng.* **3**(03), 919–926 (1988).
- ¹³LeVeque, R. J., *Numerical Methods for Conservation Laws*, 2nd ed. (Birkhauser Verlag, 1992).
- ¹⁴Meulenbroek, B., Farajzadeh, R., and Bruining, H., “The effect of interface movement and viscosity variation on the stability of a diffusive interface between aqueous and gaseous CO₂,” *Phys. Fluids* **25**(7), 074103 (2013).
- ¹⁵Namdar Zanganeh, M., Kraaijevanger, J. B. F. M., Buurman, H. W., Jansen, J. D., Rossen, W. R., and Zanganeh, M. N., “Challenges in adjoint-based optimization of a foam EOR process,” *Comput. Geosci.* **18**(3-4), 563–577 (2014).
- ¹⁶Riaz, A. and Tchelepi, H. A., “Linear stability analysis of immiscible two-phase flow in porous media with capillary dispersion and density variation,” *Phys. Fluids* **16**(12), 4727–4737 (2004).
- ¹⁷Riaz, A. and Tchelepi, H. A., “Influence of relative permeability on the stability characteristics of immiscible flow in porous media,” *Transp. Porous Media* **64**(3), 315–338 (2006).
- ¹⁸Riaz, A. and Tchelepi, H. A., “Numerical simulation of immiscible two-phase flow in porous media,” *Phys. Fluids* **18**(1), 014104 (2006).
- ¹⁹Riaz, A. and Tchelepi, H. A., “Stability of two-phase vertical flow in homogeneous porous media,” *Phys. Fluids* **19**(7), 072103 (2007).
- ²⁰Riaz, A., Hesse, M., Tchelepi, H. A., and Orr, F. M., “Onset of convection in a gravitationally unstable diffusive boundary layer in porous media,” *J. Fluid Mech.* **548**(-1), 87–111 (2005).
- ²¹Rossen, W. R., “Numerical challenges in foam simulation: A review,” in *SPE Annual Technical Conference and Exhibition, New Orleans* (SPE International, 2013).
- ²²Rossen, W. R. and Shan, D., “Optimal injection strategies for foam IOR,” *SPE J.* **9**(02), 132–150 (2004).
- ²³STARS Reservoir Simulator, *Version 2014 User Guide* (Computer Modeling Group, Calgary, Alberta, 2014).
- ²⁴Toro, E. F., *Riemann Solvers and Numerical Methods for Fluid Dynamics*, 3rd ed. (Springer, Berlin, Heidelberg, 2009).
- ²⁵Van der Meer, J. M., Van Odyck, D. E. A., Wirnsberger, P., and Jansen, J. D., “High-order simulation of foam enhanced oil recovery,” in *Proceedings of the 14th European Conference on Mathematics in Oil Recovery (ECMOR XIV)* (European Association of Geoscientists and Engineers (EAGE), Catania, 2014), pp. 8–11.
- ²⁶Van der Meer, J. M., Kraaijevanger, J. B. F. M., Möller, M., and Jansen, J. D., “Temporal oscillations in the simulation of foam enhanced oil recovery,” in *Proceedings of the 15th European Conference on Mathematics in Oil Recovery (ECMOR XIV)*, Amsterdam, 2016.
- ²⁷Wirnsberger, P., “The grid orientation effect in miscible displacement,” M.Phil. dissertation (University of Cambridge, 2012).
- ²⁸Yahya Afiff, I., “Reservoir simulation of foam flow using Kepler GPU,” M.Sc. thesis, Delft University of Technology, 2014.
- ²⁹Yortsos, Y. and Hickernell, F. J., “Linear stability of immiscible displacement processes in porous media,” *SIAM J. Appl. Math.* **49**(3), 730–748 (1989).